

## RESEARCH ARTICLE

10.1002/2015JB011951

## Key Points:

- Mantle relaxation is dominant after 2004 Sumatra-Andaman earthquake
- GPS and GRACE gravity data suggest different viscosities above and below slab
- Postseismic relaxation GRACE data slower than GPS time series from back arc

## Supporting Information:

- Table S1
- Table S2
- Figure S1
- Figure S2
- Text S1

## Correspondence to:

T. Broerse,  
d.b.t.broerse@tudelft.nl

## Citation:

Broerse, T., R. Riva, W. Simons, R. Govers, and B. Vermeersen (2015), Postseismic GRACE and GPS observations indicate a rheology contrast above and below the Sumatra slab, *J. Geophys. Res. Solid Earth*, 120, 5343–5361, doi:10.1002/2015JB011951.

Received 12 FEB 2015

Accepted 9 JUN 2015

Accepted article online 12 JUN 2015

Published online 24 JUL 2015

## Postseismic GRACE and GPS observations indicate a rheology contrast above and below the Sumatra slab

Taco Broerse<sup>1</sup>, Riccardo Riva<sup>1</sup>, Wim Simons<sup>2</sup>, Rob Govers<sup>3</sup>, and Bert Vermeersen<sup>1,2,4</sup>
<sup>1</sup>Department of Geosciences and Remote Sensing, Delft University of Technology, Delft, Netherlands, <sup>2</sup>Faculty of Aerospace Engineering, Delft University of Technology, Delft, Netherlands, <sup>3</sup>Department of Geosciences, Utrecht University, Utrecht, Netherlands, <sup>4</sup>NIOZ, Texel, Netherlands

**Abstract** More than 7 years of observations of postseismic relaxation after the 2004 Sumatra-Andaman earthquake provide an improving view on the deformation in the wide vicinity of the 2004 rupture. We include both Gravity Recovery and Climate Experiment (GRACE) gravity field data that show a large postseismic signal over the rupture area and GPS observations in the back arc region. With increasing time GPS and GRACE show contrasting relaxation styles that were not easily discernible on shorter time series. We investigate whether mantle creep can simultaneously explain the far-field surface displacements and the long-wavelength gravity changes. We interpret contrasts in the temporal behavior of the GPS-GRACE observations in terms of lateral variations in rheological properties of the asthenosphere below and above the slab. Based on 1-D viscoelastic models, our results support an (almost) order of magnitude contrast between oceanic lithosphere viscosity and continental viscosity, which likely means that the low viscosities frequently found from postseismic deformation after subduction earthquakes are valid only for the mantle wedge. Next to mantle creep, we also consider afterslip as an alternative mechanism for postseismic deformation. We investigate how the combination of GRACE and GPS data can better discriminate between different mechanisms of postseismic relaxation: distributed deformation (mantle creep) versus localized deformation (afterslip). We conclude that the GRACE-observed gravity changes rule out afterslip as the dominant mechanism explaining long-wavelength deformation even over the first year after the event.

## 1. Introduction

During the megathrust 2004  $M_w \sim 9.1$  Sumatra-Andaman earthquake, coseismic displacements have been measured by GPS at distances up to 1500 km of the epicenter, in Indonesia, Malaysia, and Thailand [Vigny *et al.*, 2005]. In the months and years after this event and the nearby 2005  $M_w \sim 8.6$  Nias earthquake large ongoing postseismic displacements have been observed throughout the same region [see, for example, Panet *et al.*, 2010; Paul *et al.*, 2012]. Initial displacement rates are fast and converge slowly to more steady velocities, which we show to be still clearly deviating from the observed preseismic motions. Integrated over more than 7 years, it shows that postseismic displacements even surpass coseismic displacements by a factor of 2 in the far field. Besides, as postseismic deformation implies an ongoing redistribution of mass, postseismic trends in the Earth's gravity field have been observed in the monthly global gravity fields produced by the Gravity Recovery and Climate Experiment (GRACE) satellite mission [e.g., Chen *et al.*, 2007; Ogawa and Heki, 2007].

Even though postseismic deformation of the solid Earth can only be measured at the surface, observations of the surface motions and gravity changes combined with numerical modeling can tell us more about deformation of the otherwise inaccessible lithosphere and mantle. Postseismic deformation is a reaction to the rupturing of a fault, relaxing coseismic stresses. Two dominant mechanisms in which the Earth relaxes these stresses are frequently proposed in literature: volume relaxation and localized afterslip. Volume relaxation occurs when the ductile upper mantle (or asthenosphere) underneath an elastic lithosphere causes widely distributed viscoelastic flow, which in turn drags the overlying lithosphere with it. Viscoelastic (volume) relaxation after the Sumatra-Andaman earthquake has been frequently proposed to explain the observed postseismic motions [e.g., Pollitz *et al.*, 2006]. Furthermore, the same mechanism has been used to explain related postseismic changes in the Earth's gravity field as measured by the GRACE [e.g., Han *et al.*, 2008].

The second (and supporting information) explanation for the observed postseismic deformation is that the ruptured fault, or its updip or downdip continuation, can continue to slip slowly after the rupture has stopped;

thus causing localized afterslip [e.g., *Barbot et al.*, 2009]. Some parts of the fault, characterized by their velocity strengthening frictional behavior, do not allow fast propagation of the rupture. However, these areas can be forced to slip aseismically after coseismic slip has drastically changed stress conditions on nearby velocity-weakening parts of the fault [e.g., *Scholz*, 1998]. Related to afterslip is the occurrence of aftershocks, which are often assumed to have a comparable decaying rate as afterslip [e.g., *Perfettini and Avouac*, 2004; *Hsu et al.*, 2006]. Aftershocks are thought to be induced by afterslip, as afterslip transfers stress to those parts of the fault that are again locked after the main event [e.g., *Perfettini and Avouac*, 2007; *Helmstetter and Shaw*, 2009], although aftershocks have also been explained as resulting from stress changes due to transient creep [*Savage et al.*, 2007]. While aftershocks came in large numbers after the 2004 event, their cumulative seismic moment is relatively small; up to mid-February 2005 a total aftershock moment release of  $M_w \sim 7.5$  has been estimated [*Bilham et al.*, 2005], which is less than 1% of the seismic moment needed to explain postseismic displacements in the first month [*Chlieh et al.*, 2007]. Hence, while the study of aftershocks is important for understanding frictional properties of faults, in contrast to contributions of afterslip or viscoelastic relaxation, their contribution to postseismic deformation is often very small [*Perfettini and Avouac*, 2007; *Chlieh et al.*, 2007; *Ozawa et al.*, 2012].

Both volume relaxation and localized afterslip are likely to occur after large earthquakes; only their relative contribution to the observed postseismic deformation and the time at which they act are still debated, both for the specific case of the Sumatra-Andaman event [*Panet et al.*, 2010; *Hoechner et al.*, 2011; *Hu and Wang*, 2012; *Paul et al.*, 2012] or more in general [*Bürgmann and Dresen*, 2008, and references therein]. Postseismic relaxation may also be affected by the complex interior geometry of subduction zones as well as a potential viscosity contrast between suboceanic asthenosphere and the mantle wedge [*Pollitz et al.*, 2008]. Using models of viscoelastic flow and afterslip, the observed displacements can be used to study the deforming mechanisms and the rheology, the flow properties, of the upper mantle. More broadly, a better understanding (and measurement) of the deformation seen in the wake of large earthquakes can improve our knowledge about stress transfer during the earthquake cycle.

We integrate up to 7 years of far-field GPS and more than 7 years of GRACE observations, to get an unprecedented overview of the regional-scale pattern of postseismic relaxation. In contrast to previous studies that infer a relaxation pattern from GRACE that suggests that most relaxation occurred already in the first 4 years [e.g., *Han et al.*, 2008; *de Linage et al.*, 2009; *Hoechner et al.*, 2011], we show that postseismic relaxation is still ongoing. Since we can now better constrain postseismic trends and, compared to GPS-only postseismic studies, including global GRACE gravity field changes expands the sensitivity to relaxation in the suboceanic asthenosphere, we address the following questions:

1. Can the combination of GRACE and GPS make a distinction between localized and distributed deformation after the 2004 Sumatra-Andaman earthquake? And, if distributed deformation is the major deformation mechanism:
2. Do the combined GRACE and GPS data indicate different viscosities in the suboceanic asthenosphere and in the mantle wedge?

## 2. Previous Studies

A number of studies succeed relatively well in explaining the first few years of postseismic deformation after the two Sumatra events with a biviscous Burgers rheology [e.g., *Pollitz et al.*, 2006; *Hoechner et al.*, 2011]. On the other hand, the common univiscous Maxwell model seems not to be able to reproduce the transient postseismic signal [e.g., *Paul et al.*, 2007]. With a Burgers rheology, a fraction of the elastic strain energy relaxes due to viscous flow with a low viscosity ( $\eta_k$ ), and the remaining elastic strain energy decays due to flow at a higher viscosity ( $\eta_m$ ). Laboratory experiments confirm that steady state (nonrecoverable) creep is preceded by faster (and fully recoverable) transient creep [*Chopra*, 1997; *Gribb and Cooper*, 1998; *Lakki et al.*, 1998; *Faul and Jackson*, 2005]. Postseismic relaxation after the 2004 event is often explained using steady state viscosities in the range  $\eta_m = 5 \cdot 10^{18}$  to  $1 \cdot 10^{19}$  Pa s together with an order of magnitude smaller transient viscosities, summarized in Table 1. Commonly, models feature viscosities of  $\eta_m = 10^{20}$  Pa s in the upper mantle below 220 km and an order of magnitude higher viscosity in the lower mantle (below 670 km). Some studies combine viscoelastic relaxation with afterslip to explain postseismic relaxation [*Panet et al.*, 2010; *Hu and Wang*, 2012; *Paul et al.*, 2012], while *Hoechner et al.* [2011] find that significant afterslip is not needed to explain GPS and GRACE observations in the 4 years after the 2004 event.

**Table 1.** Viscosity Values From a Selection of Studies Investigating the Postseismic Relaxation Following the 2004 Sumatra-Andaman Earthquake Using a Burgers Rheology

	$\eta_m$ (Pa s)	$\eta_k$ (Pa s)	Depth Range Asthenosphere (km)	Period GPS <sup>a</sup> (years)	Period GRACE (years)	Comments
<i>Pollitz et al.</i> [2006]	$1 \cdot 10^{19}$	$5 \cdot 10^{17}$	62–220	0.3	-	
<i>Pollitz et al.</i> [2008]	$1 \cdot 10^{19}$	$5 \cdot 10^{17}$	50/62–220	1	-	including slab; mantle wedge viscosities: $0.4 \cdot \eta$
<i>Han et al.</i> [2008]	$5-10 \cdot 10^{18}$	$5 \cdot 10^{17}$	62–220	-	2.3	
<i>Panet et al.</i> [2010]	$8 \cdot 10^{18}$	$4 \cdot 10^{17}$	60–220	3.5	2.75	220–670 km depth: $\eta_m = 8 \cdot 10^{18}$ Pa s; including afterslip
<i>Hoechner et al.</i> [2011]	$1 \cdot 10^{19}$	$1 \cdot 10^{18}$	40–210	1.5/3	4	no afterslip needed
<i>Hu and Wang</i> [2012]	$1 \cdot 10^{19}$	$5 \cdot 10^{17}$	62–220	1.5/3	-	including slab and afterslip; oceanic asthenosphere: $\eta_m = 1 \cdot 10^{19}$ Pa s

<sup>a</sup>When for the period of the GPS data two numbers are given the first number denotes the period of near-field observations and the second the period of the far-field observations.

At the Sumatra subduction zone the Indian and Australian plates subduct below the Sunda plate [Simons *et al.*, 2007]. During subduction of oceanic lithosphere, dehydration of the descending slab transports water into the overlying mantle [e.g., Karato, 2011]. This may have some implications for the rheology of the mantle wedge, the part of the mantle between the sinking slab and the overriding continental lithosphere, as water content decreases viscosity compared to surrounding asthenosphere viscosity [Hirth and Kohlstedt, 2003; Dixon *et al.*, 2004]. Nevertheless, early (2 to 4 years) postseismic GPS measured back arc displacements next to postseismic GRACE gravity changes seem to be explained rather well using laterally homogeneous models [Han *et al.*, 2008; Panet *et al.*, 2010; Hoechner *et al.*, 2011] (where Han *et al.* [2008] only consider GRACE data). In the case of the 2004 Sumatra-Andaman earthquake, only Pollitz *et al.* [2008] and Hu and Wang [2012] model lateral variations in viscosity. Next to introducing a high-viscosity subducting slab, Pollitz *et al.* [2008] add a 40% viscosity contrast between the oceanic asthenosphere and the low viscous mantle wedge below the continent, while Hu and Wang [2012] implement an order of magnitude contrast for the steady state viscosity. Both studies confront their laterally heterogeneous models with GPS-observed land displacements close to the fault at the Andaman islands and on the Malaysian Peninsula, using approximately 1 and 3 years of observations, respectively. However, it is not yet clear whether the postseismic relaxation data actually require a lateral viscosity contrast of the subslab and supraslab asthenosphere, due to the limited sensitivity of land displacements to the suboceanic lithosphere [Hu *et al.*, 2004].

### 3. GPS Observed Displacements

#### 3.1. Processing

We use horizontal GPS data from 11 permanent and campaign sites throughout Thailand, located in the back arc of the northern part of the Sunda subduction zone, minimally 400 km easterly from the trench. All have experienced observable coseismic [Vigny *et al.*, 2005] and postseismic displacements throughout the measurement period of maximum 7 years after the event. As vertical deformation decreases faster with increasing distance to the fault and noise levels are higher, for vertical displacements we use a smaller subset of two permanent GPS sites that are relatively close to the rupture and that were operational during the earthquake. While more recent GPS data are available, the 2012 Indian Ocean earthquake caused extra coseismic and, likely postseismic displacements, that complicate the analysis of the postseismic displacements in Thailand due to the 2004 event. Closer to the 2004 rupture, at the Andaman and Nicobar islands approximately 100 km from the trench, several GPS sites have been installed in the 2 to 6 weeks after the event [Gahalaut *et al.*, 2006] and more than 6 years of postseismic data have been collected [Paul *et al.*, 2012]. Due to the absence of measurements directly after the earthquake, the first 20–40 days of postseismic displacements cannot be distinguished from the purely coseismic position jumps, which means that a large part of

the initial near-field postseismic signal cannot be observed. Namely, according to *Vigny et al.* [2005] in the first 50 days after the event Phuket moved as much as 25% of the coseismic displacement.

Next to the considerable bias in the postseismic time series, near-field sites are more sensitive to local effects, such as poroelastic deformation [*Hughes et al.*, 2010]. Furthermore, the near field is susceptible to variations in slip along strike: postseismic GPS vectors show strong variations in direction over small distances at the Andaman and Nicobar islands [*Paul et al.*, 2012], while far-field vectors point all in the direction of the epicenter. For these reasons we leave the near-field data aside for now and focus on the far-field GPS sites.

All GPS data are processed with GIPSY-OASIS II, using the Precise Point Positioning strategy [*Zumberge et al.*, 1997]. Weekly averaged solutions are subsequently mapped onto the ITRF 2005 frame [*Altamimi et al.*, 2007] and interseismic plate motions according to *Simons et al.* [2007] are removed. The supporting information Table S1 contains the residuals for the preearthquake period and the estimated linear interseismic velocities. Furthermore, we provide in supporting information Table S2 the available positions for the preearthquake and postearthquake periods with the interseismic velocities subtracted (shown in supporting information Figures S1 and S2 for sites PHUK and BNKK). To preserve postseismic motions only, we subtract coseismic displacements calculated for the 2004 Sumatra-Andaman earthquake as published in *Vigny et al.* [2005] and subsequent 2005 Nias and the 12 and 13 September 2007 Bengkulu earthquakes. At some locations where sites have been discontinued and nearby stations have continued observations, we recombine (i.e., average) postseismic time series from these sites into a new time series. Since time series show overlap, no data gaps are introduced. We combine sites PHKT and PTCT as well as the sites BNKK, CUSV, and RTSD. Since CPNT was installed shortly after the earthquake, we use the coseismic displacement of nearby site BANH.

Uncertainties of the time series are computed by

$$\sigma_{\text{post}} = \sqrt{\sigma_p^2 + \sigma_{\text{ref}}^2 + (t - t_{\text{SA}})^2 \sigma_v^2 + H(t - t_{\text{SA}}) \sigma_{\text{SA}}^2 + H(t - t_{\text{N}}) \sigma_{\text{N}}^2 + H(t - t_{\text{B}}) \sigma_{\text{B}}^2} \quad (1)$$

Here  $\sigma_p$  denotes the standard deviation of the weekly solution,  $\sigma_{\text{ref}}$  and  $\sigma_v$  the standard deviations of the reference position and reference velocity at 25 December 2004,  $H(t - t_{\text{earthquake}})$  are Heaviside step functions,  $t$  is time,  $t_{\text{SA}}$ ,  $t_{\text{N}}$ , and  $t_{\text{B}}$  are the epochs of the subsequent seismic events (2004 Sumatra-Andaman, 2005 Nias, and 2007 Bengkulu, respectively) and finally  $\sigma_{\text{SA}}$ ,  $\sigma_{\text{N}}$ , and  $\sigma_{\text{B}}$  are the standard deviations of the coseismic displacements.

### 3.2. Analysis of Postseismic Displacements

Comparison between observations and model results is facilitated by fitting a trend through the time series such that relaxation time and total postseismic displacement at uniform epochs can be determined. Because of the clear transient in the postseismic deformation, which may either hint at relaxation of a Burgers body or afterslip, a logarithmically decaying function fits such a curve quite well, as shown by *Hetland and Hager* [2006]

$$y(t) = a \ln \left( 1 + \frac{t}{\tau_{\text{ln}}} \right) \quad (2)$$

We solve this equation using nonlinear least squares. Here  $y(t)$  is the estimated displacement,  $a$  a scaling constant,  $t$  time in years since the event, and  $\tau_{\text{ln}}$  the (phenomenological) logarithmic relaxation time. Small values of  $\tau_{\text{ln}}$  indicate a strong initial slope with respect to later epochs, whereas large values of  $\tau$  indicate trends with little variation in slope.

## 4. GRACE

To study long wavelength postseismic changes in the gravity field around the 2004 rupture, we make use of the monthly GRACE gravity solutions by CSR (Level-2, release 5 data) [*Bettadpur*, 2012], spanning a period between January 2003 and March 2012. While more GRACE data are available, we prefer to exclude contamination of the time series due to gravitational changes of the 2012 Indian Ocean earthquake [*Han et al.*, 2013]. We downward continue the gravity fields by 7 km to 6371 km and convert the GRACE Stokes coefficients  $C_l^m$  to gravity anomaly coefficients by

$$\Delta g_l^m = \frac{GM}{r^2} (l - 1) C_l^m \quad (3)$$

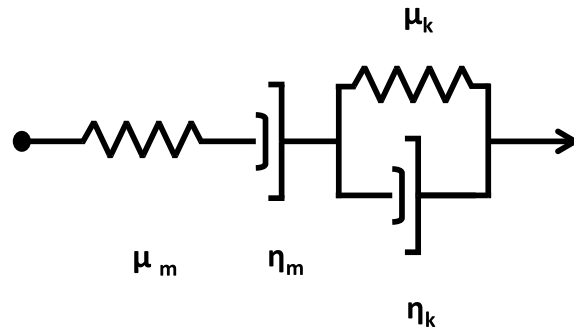


**Figure 1.** Schematic representation of a Burgers rheology, consisting of a Maxwell element in series with a Kelvin element where a dashpot and spring are connected in parallel. Viscosity is denoted by  $\eta$  and shear modulus by  $\mu$  (subscripts m and k denote the Maxwell and Kelvin parameters, respectively). The Maxwell element results in elastic deformation and steady state creep, while the Kelvin element results in transient creep that dominates directly after load changes.

with the gravitational constant  $G$ , the Earth's mass  $M$ , the Earth's radius  $r$ , and degree  $l$  and order  $m$ . Through these monthly gravity fields we fit, using nonlinear least squares, the same logarithmically decaying function as utilized for the GPS time series (equation (2)) to obtain the postseismic signal. Because of the monthly combinations of data, the coseismic gravity change is best estimated simultaneously with a postseismic trend. Alongside earthquake-induced gravity changes we estimate hydrological annual and semiannual seasonal and the S2 tidal aliasing signals [Ray and Luthcke, 2006]. Our fitting function then becomes

$$y = a \cos(2\pi t) + b \sin(2\pi t) + c \cos(2\pi \omega t) + d \sin(2\pi \omega t) + e \cos(4\pi t) + f \sin(4\pi t) + g + H(t - t_{eq}) \left( h + i \ln \left( 1 + \frac{t - t_{eq}}{\tau_{ln}} \right) \right) \quad (4)$$

where  $a$  to  $i$  are constants,  $\omega$  is 365/161, being the 161 day S2 tidal alias phase,  $H$  is the Heaviside function,  $t$  is the time in years, and  $t_{eq}$  is the time of the earthquake. In this way  $h$  is the coseismic discontinuity for each grid point,  $i$  a scaling factor, and  $\tau_{ln}$  the (phenomenological) logarithmic relaxation time. We determine uncertainties a posteriori, based on the fit to the data. Since  $\tau_{ln}$  can only be reliably estimated at those locations where there is a large postseismic signal, we first estimate  $\tau$  at the locations with the largest positive and negative postseismic signal (where we allow it to vary between 0.5 and 10 years) and subsequently constrain  $\tau$  for the larger region to be within this interval. We estimate the confidence intervals of the postseismic trend by fixing the coseismic discontinuity at its 95% confidence boundaries.

## 5. Viscoelastic Relaxation Model

To compute solid Earth deformation and gravity potential changes we use the analytical normal mode method [Vermeersen and Sabadini, 1997; Sabadini and Vermeersen, 2004], which treats the Earth as a radially stratified, compressible, and self-gravitating spherical body. The viscoelastic response is based on the biviscous Burgers body that allows for two different phases of creep: transient and steady state (Figure 1). The implementation in the normal modes approach is described in Appendix A. Elastic Earth properties are derived from preliminary reference Earth model (PREM) [Dziewonski and Anderson, 1981]. We model slip using seismic point sources [Smylie and Mansinha, 1971; Piersanti et al., 1995], including corrections for seismic forcing given by Cambiotti et al. [2011].

We form a series of spherically stratified Earth models that include (1) a purely elastic lithosphere with a thickness  $D_l$  of either 40, 60, or 80 km, (2) a low-viscosity asthenosphere down to 220 km depth, and (3) the remaining upper mantle between 220 and 670 km depth, on top of (4) a high viscosity lower mantle layer which extends to the core at 2891 km depth (Table 2).

Furthermore, we also test for various ratios of Kelvin shear modulus to Maxwell shear modulus:  $\gamma = \frac{\mu_k}{\mu_m}$ . Except Hoechner et al. [2011] all other publications studying the Sumatra-Andaman postseismic relaxation that we are aware of assume that  $\mu_k = \mu_m$ , while it is likely that the Kelvin element is slightly weaker than the Maxwell element [Hetland and Hager, 2006]. As input for the Sumatra-Andaman slip distribution we use the  $G-M 9.15$  model by Chlieh et al. [2007]. This slip model is based on far-field and (downscaled) near-field GPS measurements, in situ and remote observations of coral reef vertical motions, includes tsunami modeling, and is checked for consistency with normal modes and with the amplitude of very long period surface waves.



**Table 2.** Parameters for the Viscoelastic Earth Model, Volume-Averaged From PREM [Dziewonski and Anderson, 1981] (200 s Reference Period); With the Upper Boundary Radius, the Depth of the Lower Extent of the Layer, the Density of the Layer  $\rho$ , the Shear Modulus  $\mu$ , the Maxwell and Kelvin Viscosities  $\eta_m$  and  $\eta_k$ , and the First Lamé Parameter  $\lambda$

Name	Radius (km)	Depth (km)	$\rho$ (kg/m <sup>3</sup> )	$\mu_m$ (N/m <sup>2</sup> )	$\eta_m$ (Pa s)	$\eta_k$ (Pa s)	$\lambda$ (N/m <sup>2</sup> )
Elastic lithosphere	6,371	24	2,732	$0.341 \cdot 10^{11}$	$\infty$	$\infty$	$0.395 \cdot 10^{11}$
	6,347	40–80	3,380	$0.677 \cdot 10^{11}$	$\infty$	$\infty$	$0.858 \cdot 10^{11}$
Asthenosphere	6,331–6,291	220	3,370	$0.668 \cdot 10^{11}$	$\eta_{m,a}$	$\eta_{k,a}$	$0.840 \cdot 10^{11}$
Upper mantle < 220 km depth	6,151	670	3,698	$0.94 \cdot 10^{11}$	$1 \cdot 10^{20}$	$\infty$	$1.42 \cdot 10^{11}$
Lower mantle	5,701	2,891	4,878	$2.19 \cdot 10^{11}$	$1 \cdot 10^{21}$	$\infty$	$3.13 \cdot 10^{11}$
Core	3,480	6,371	10,932	-	-	-	-

Figure 2 shows that our model reproduces coseismic displacements well and that displacements due to the 2005 Nias earthquake are very small for the selected GPS sites.

We visually inspect the completeness of each model for all known modes, including the stronger dilatation modes (shown in Appendix A). Furthermore, the models are solved up to  $l_{\max} = 450$ , where a cosine taper is applied for the degree range 300–450. This successfully removes truncation errors, which would otherwise manifest as small wavelength oscillations with considerable amplitudes in the far field. We check that the application of a taper starting at degree 300 does not remove any real contribution to the deformation in areas where GPS observations have been taken.

### 5.1. Modeling Gravity Changes

For modeling gravity field changes, next to the normal modes solid Earth model, we also apply the sea level equation for seismic perturbations [Melini et al., 2010; Broerse et al., 2011, 2014]. Here we apply the sea level equation in the elastic mode, meaning that we omit any solid Earth relaxation due to changes in the water column. As in the coseismic case, any relaxation due to sea level changes can be discarded for the postseismic case, since elastic deformation due to relative sea level changes is at the 1% level of the maximum deformation

due to slip itself [Broerse et al., 2014]. Only relaxation due to the 2004 event is modeled, as the 2005 Nias earthquake has a very small influence due to its 7 times lower seismic moment. The sea level equation is solved up to degree and order 450, such that coast lines can be properly accounted for. After the solution has converged, geoid anomalies  $N$  are converted into gravity anomalies  $\Delta g$  in the spherical harmonic domain by

$$\Delta g_l^m = \frac{GM}{r^3} (l-1) N_l^m \quad (5)$$

and the series are truncated at  $l_{\max} = 40$  for comparison with GRACE.

## 6. Distributed Deformation: Mantle Creep

### 6.1. Comparison of GPS Observations With Model

To compare the postseismic GPS time series with our mantle relaxation model we select seven sites that have long (5–7 years) observation spans with an even distribution over the area: PHUK, CPNT, RYNG, RTSD, SRIS, UTHA, and OTRI. We do not include stations south of

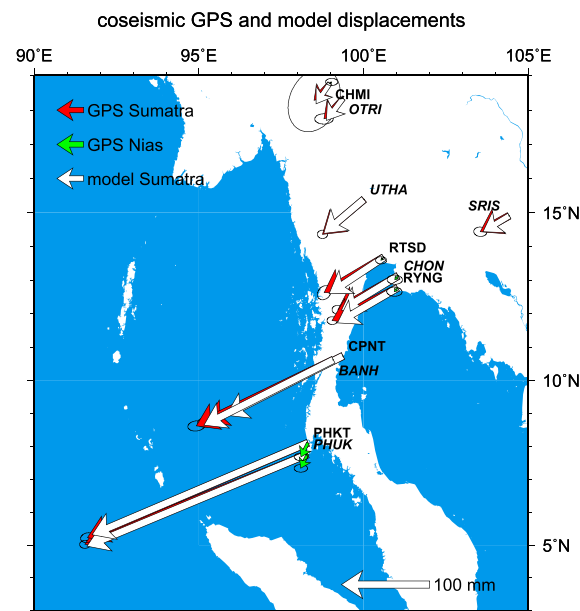


**Figure 2.** Comparison between observed coseismic GPS displacements due to the Sumatra-Andaman earthquake and predicted model displacements based on the Chlieh et al. [2007]  $G-M$  9.15 slip distribution model. Also included are estimated 2005 Nias coseismic displacements (only visible for sites PHUK/PHKT). Confidence ellipses are given at 95%. Names of campaign sites are shown in italics.

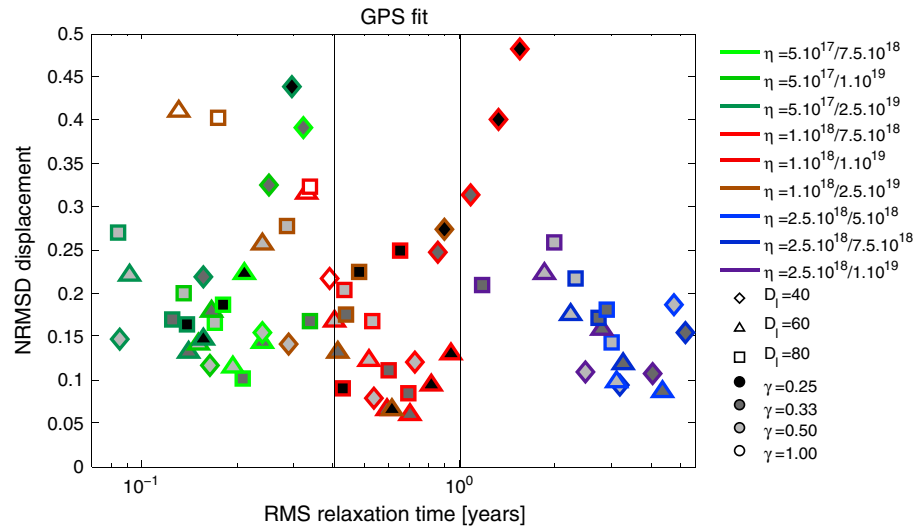


**Figure 3.** Viscoelastic model misfits with GPS; on the logarithmic  $x$  axis relaxation time  $\tau$  (equation (1)) and on the  $y$  axis the normalized root-mean-square deviation (NRMSD). Nine different viscosity combinations are included, shown in the legend as transient/steady state viscosities (Pa s). Green colors represent models with transient viscosity  $\eta_k = 5 \cdot 10^{17}$  Pa s, red and brown represent models with transient viscosity  $\eta_k = 1 \cdot 10^{18}$  Pa s, and blue colors stand for models with transient viscosity  $\eta_k = 2.5 \cdot 10^{18}$  Pa s. For each transient viscosity, three different steady state viscosities  $\eta_m$  have been modeled. Symbol denotes the lithospheric thickness  $D_l$  while its fill shows the shear modulus ratio  $\gamma$ . The vertical straight lines show the range of relaxation times  $\tau$  as estimated from the GPS time series. Small values of  $\tau_{in}$  indicate a strong initial slope with respect to later epochs, whereas large values of  $\tau$  indicate trends with little variation in slope.

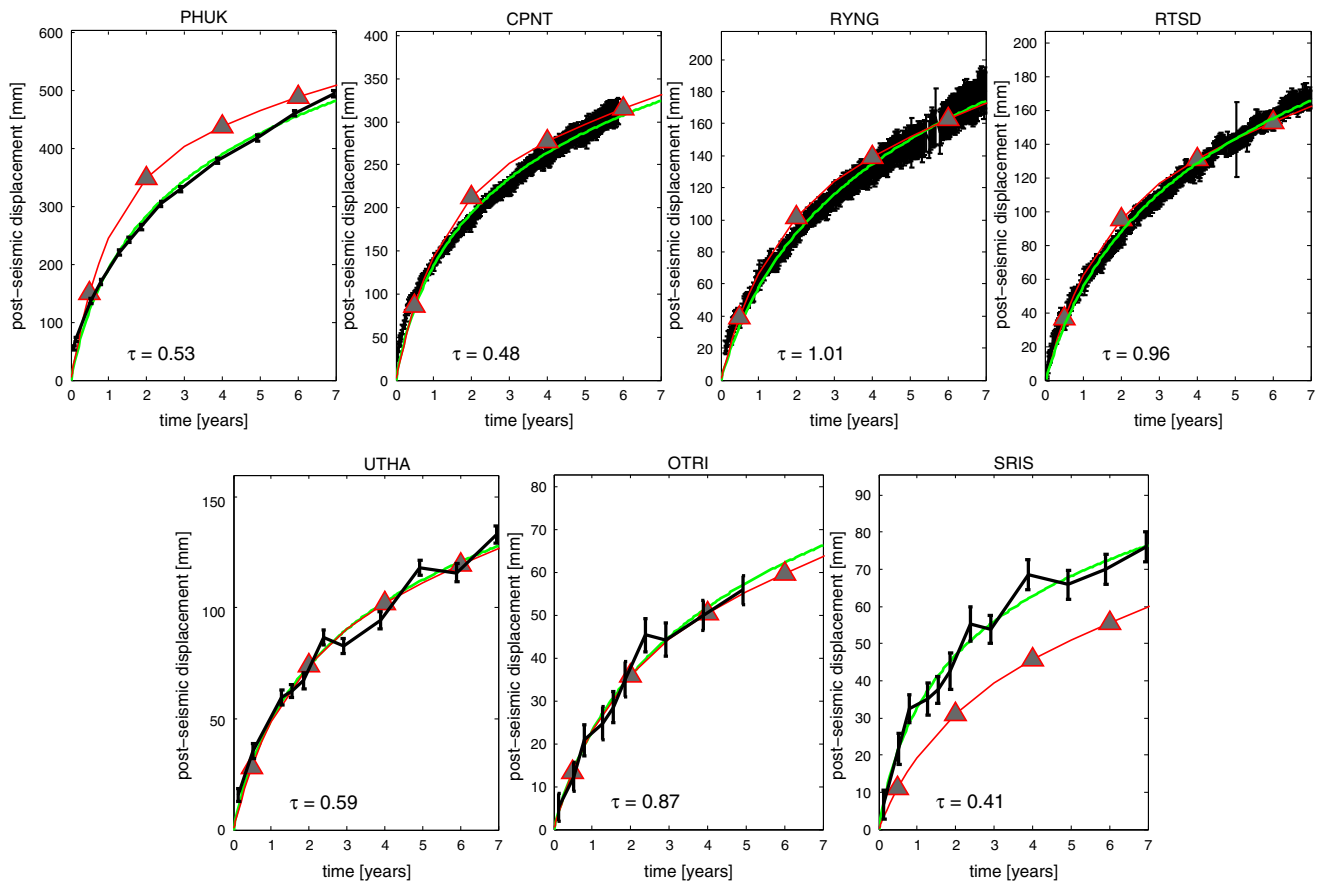
Phuket in order to minimize influence of the 2005 Nias earthquake. One outlier is removed for site OTRI, where the last campaign measurement is otherwise responsible for doubling the relaxation time. We select the best fitting model based on the model relaxation time  $\tau$  and the normalized root-mean-square deviation (normalized to increase the influence of far-field sites that are subject to relatively small displacements). The normalized root-mean-square deviation (NRMSD) is defined by

$$NRMSD = \frac{1}{\sqrt{n}} \sqrt{\sum_i^s \sum_j^m \left( \frac{\sqrt{(E_{GPS,j} - E_{model,j})^2 + (N_{GPS,j} - N_{model,j})^2}}{|x|_{max,i}} \right)^2} \quad (6)$$

where  $n$  is the total number of observations over all GPS sites,  $s$  the number of sites,  $m$  the number of observations per site,  $E$  and  $N$  the postseismic displacements in east and north directions, respectively, and  $|x|_{max,i}$  the maximum absolute horizontal displacement at site  $i$ . Figure 3 shows the NRMSD and RMS of the modeled relaxation time  $\tau$  compared to the GPS-derived relaxation times.

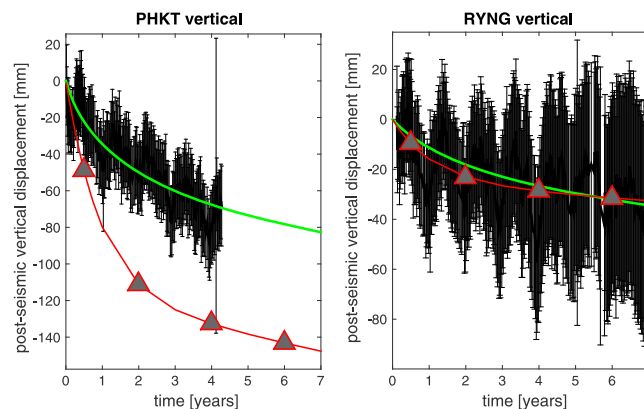
Starting with relaxation times, as the relaxation times  $\tau$  of the GPS time series are all in the 0.4–1 year range, we can already make a selection of feasible viscosity combinations. From Figure 3 we can see that the relaxation time  $\tau$  is mostly dependent on the transient viscosity  $\eta_k$  and slightly decreases when the difference between transient and steady state viscosity becomes larger. Additionally, a decrease in  $\tau$  can be seen when the contribution of the transient deformation increases due to a higher Kelvin shear modulus (higher  $\gamma$ ). Figure 3 clearly shows that the most promising models include a transient viscosity  $\eta_k$  of  $1 \cdot 10^{18}$  Pa s. Thus, we can discard transient viscosities of  $\eta_k$  of  $5 \cdot 10^{17}$  Pa s and lower, and transient viscosities of  $\eta_k$  of  $2.5 \cdot 10^{18}$  Pa s and higher, since these models cannot reproduce the curvature of the time series, expressed in terms of  $\tau$ . Steady state viscosities are not as well constrained, as  $\eta_m$  values between  $7.5 \cdot 10^{18}$  Pa s and  $2.5 \cdot 10^{18}$  Pa s can all reproduce the  $\tau$  values as estimated from the GPS data. Best fits for shear modulus ratio  $\gamma$  are in the 0.25–0.33 range, while a lithospheric thickness of 60 km produces the best fit for the sites closest to the rupture as well as sites located farthest away from the subduction zone.

Figure 4 illustrates that the best fit model with parameters  $\eta_k = 1 \cdot 10^{18}$ ,  $\eta_m = 7.5 \cdot 10^{18}$  Pa s, lithospheric thickness  $D_l$  of 60 km, and  $\gamma = 0.33$  explains all postseismic displacements rather well. Exceptions are site SRIS, which is the most easterly station of the network, and site PHUK, which is the site closest to the 2004 rupture.



**Figure 4.** GPS time series with  $1\sigma$  error bars. The green line shows the GPS postseismic fit, together with the best fitting model in red: asthenosphere viscosities  $\eta_k = 1 \cdot 10^{18}$ ,  $\eta_m = 7.5 \cdot 10^{18}$  Pa s, shear modulus ratio  $\gamma = 0.33$ , and lithospheric thickness  $D_l = 60$  km. Estimates for the logarithmic relaxation time  $\tau$  (in years) are shown for all selected GPS time series. Small values of  $\tau_{ln}$  indicate a strong initial slope with respect to later epochs, whereas large values of  $\tau$  indicate trends with little variation in slope.

We underpredict the displacement at SRIS, as does any other model that fits the other sites well. All models that provide a good overall fit for the whole network lead to slightly too much transient deformation for site PHUK. Figure 5 shows the time series of vertical GPS displacements of two permanent GPS sites, next to the estimated logarithmic fit, where we constrain the relaxation time to that of the horizontal fit. All featured sites show postseismic subsidence. As Figure 5 demonstrates, the model that best fits the horizontal displacements correctly reproduces the style of vertical deformation, namely, subsidence. However, the model overestimates



**Figure 5.** GPS time series of vertical displacements with  $1\sigma$  error bars. The green line shows the GPS vertical postseismic fit, together with the model that fitted the horizontal displacements best, in red: asthenosphere viscosities  $\eta_k = 1 \cdot 10^{18}$ ,  $\eta_m = 7.5 \cdot 10^{18}$  Pa s, shear modulus ratio  $\gamma = 0.33$ , and lithospheric thickness  $D_l = 60$  km.



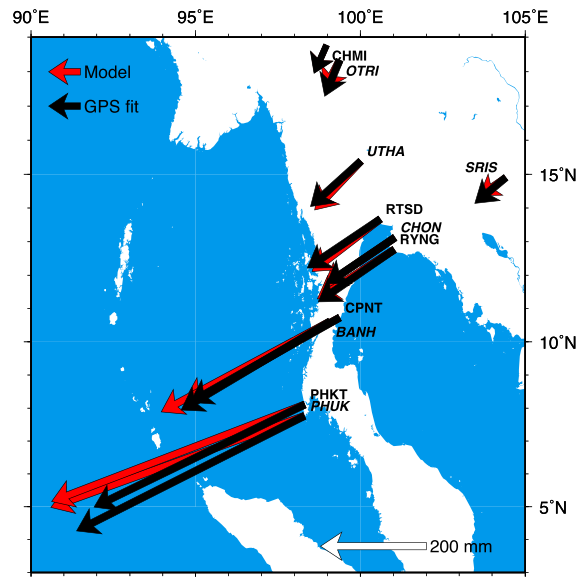


**Figure 6.** Comparison of 7 year integrated postseismic vectors of GPS (black) and the preferred viscoelastic model (red). GPS vectors are represented by the logarithmic fits. Preferred model has parameters  $\eta_k = 1 \cdot 10^{18}$ ;  $\eta_m = 7.5 \cdot 10^{18}$  Pa s;  $D_l = 60$  km;  $\gamma = 0.33$ . Site names shown in italics correspond to campaign sites.

the amount of displacement for site PHKT, while for the site farther away from the rupture, RYNG, the magnitude matches well.

Figure 6 shows that the best fit model reproduces the integrated 7 year displacements in terms of total displacement and direction. Postseismic deformation at all observed sites points in the direction of the ruptured fault, consistent with viscoelastic relaxation [e.g., Wang *et al.*, 2012], and the directions are very similar to the observed coseismic displacements (Figure 2). To understand the influence of variations in the four studied parameters, we show the effect of these on deformation of sites CPNT and OTRI in Figure B1 in Appendix B.

## 6.2. Comparison of GRACE With Model

We find a large ongoing postseismic increase of gravity over the rupture, sided by two areas that experience a decreasing trend in gravity, quite distinct from the coseismic dipole pattern (Figure 7, left). The spatial pattern of the postseismic gravity change (shown by Figure 7) is comparable to previous accounts [e.g., de Linage *et al.*, 2009; Panet *et al.*, 2010]: a dominant positive increase over the ruptured area with a smaller negative easterly, in the Gulf of Thailand, and a minor negative west of the positive increase. The pattern is clearer than

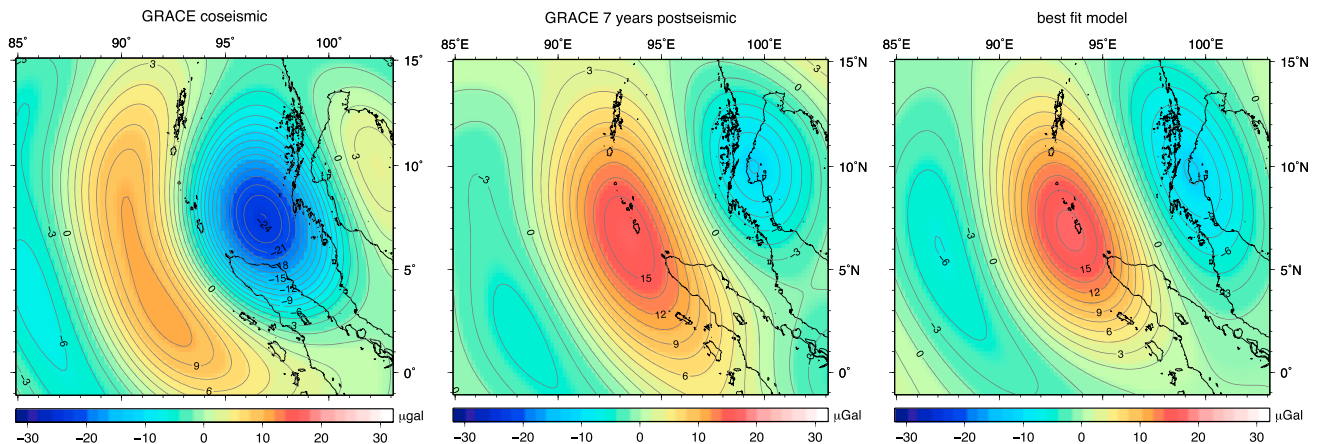


**Figure 7.** (left) Estimated GRACE coseismic gravity change due to the 2004 Sumatra-Andaman earthquake with  $I_{\max} = 40$ , using equation (4). (middle) Estimated GRACE postseismic gravity change 7 years after the 2004 Sumatra-Andaman earthquake with  $I_{\max} = 40$ , using equation (4). (right) Best fit model, with parameters  $\eta_k = 7.5 \cdot 10^{18}$  Pa s,  $\eta_m = 5 \cdot 10^{19}$  Pa s,  $D_l = 40$  km, and  $\gamma = 0.75$ ,  $I_{\max} = 40$ .

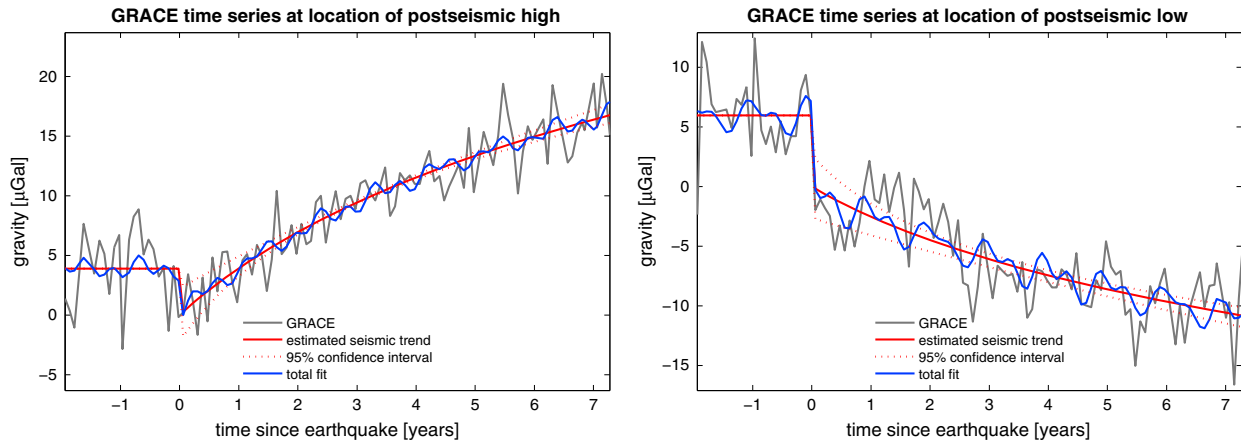


**Figure 8.** Time series of GRACE gravity anomalies and estimated seismic signals at the locations of the (left) largest positive (northwest of Aceh, Sumatra) and (right) largest negative (western Gulf of Thailand) postseismic estimates. Confidence intervals correspond to the postseismic estimate only. All gravity anomalies are truncated at spherical harmonic degree and order  $l_{\max} = 40$  and GRACE epochs are set to half way the monthly solutions.

previous accounts, due to the use of updated GRACE gravity products (release 5 data) and longer time series. We find a relatively slow transient from the gravity observations (compared to the postseismic GPS displacements), as is indicated by the time series at the location of maximum positive trend and maximum negative trend in Figure 8. Relaxation times  $\tau_{\text{in}}$  are estimated to be 2.9 years (1.2–9.8) and 5.0 years (1.5–20.8) for the positive peak and negative peak, with 95% confidence interval between brackets. While the total seismic

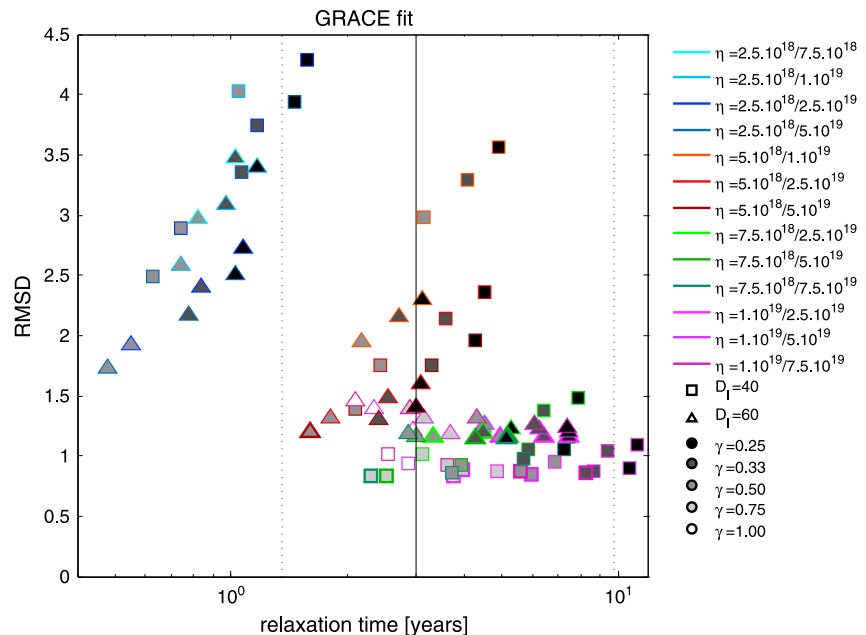


**Figure 9.** Model fits with the GRACE-derived postseismic trend; on the logarithmic  $x$  axis relaxation time  $\tau$  (equation 4) and on the  $y$  axis the mean root-mean-square deviation (RMSD) for the area depicted in Figure 7 (at epochs 0.1, 0.2, 0.3, 0.5, 0.75, 1, 2, 3, 4, 5, 6 and 7 years). Thirteen different viscosity combinations are included, shown in the legend as transient/steady state viscosities (Pa s). Blue colors represent models with transient viscosity  $\eta_k = 2.5 \cdot 10^{18}$  Pa s, red and brown represent models with transient viscosity  $\eta_k = 5 \cdot 10^{18}$  Pa s, green colors stand for models with transient viscosity  $\eta_k = 7.5 \cdot 10^{18}$  Pa s, and purple colors stand for models including a transient viscosity of  $\eta_k = 1 \cdot 10^{19}$  Pa s. For each transient viscosity, three different steady state viscosities  $\eta_m$  have been modeled. The symbol denotes the lithospheric thickness  $D_l$  while its fill shows the shear modulus ratio  $\gamma$ . The vertical straight line shows the relaxation time  $\tau$  as estimated from the GRACE gravity field at the location where the postseismic trend peaks, dotted lines show the 95% confidence interval. Small values of  $\tau_{\text{in}}$  indicate a strong initial slope with respect to later epochs, whereas large values of  $\tau$  indicate trends with little variation in slope.

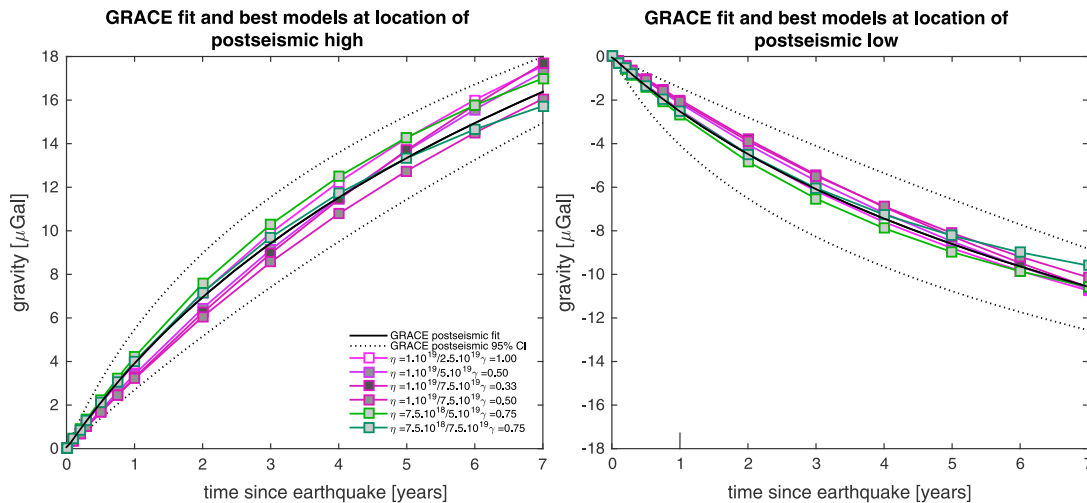


**Figure 10.** Gravity time series of the postseismic trend from GRACE and best fitting models at (left) the location of the largest positive trend (northwest of Aceh, Sumatra) and (right) the location of the largest negative trend (western Gulf of Thailand). All best fitting models have a lithospheric thickness  $D_l$  of 40 km. Confidence interval of the postseismic gravity change is given at 95%. All gravity anomalies are truncated at spherical harmonic degree and order  $l_{\max} = 40$ .

signal can be estimated quite well, the separation between coseismic and postseismic signals mainly introduces uncertainties in the rate of postseismic change.

Since we find higher relaxation times  $\tau$  for GRACE postseismic relaxation than for GPS observed surface displacements, we add a number of viscoelastic models with higher transient and steady state asthenosphere viscosities than those we used for comparison with GPS. We assess the model fit in terms of relaxation time and RMS deviation (mean of RMS deviation within the area shown in Figure 7 at epochs 0.1, 0.2, 0.3, 0.5, 0.75, 1, 2, 3, 4, 5, 6, and 7 years). Whereas we found the best fit for GPS with viscosities of  $\eta_k = 1 \cdot 10^{18}$  Pa s and  $\eta_m = 7.5 \cdot 10^{18}$  Pa s, Figure 9 shows that in order to fit the GRACE gravity changes we need higher asthenosphere viscosities. Namely, models that fit the estimated relaxation time from GRACE and have a low RMS deviation all have transient viscosities in the range  $\eta_k = 7.5 \cdot 10^{18} - 1 \cdot 10^{19}$  Pa s. While a few models with transient viscosities of  $\eta_k = 5 \cdot 10^{18}$  Pa s seem to result in a good fit in terms of relaxation time, these models (and those with even lower transient viscosities) all overpredict the total postseismic gravity change, hence the high RMS misfits. Figure 9 illustrates as well that there is a clear preference for models with a lithosphere thickness  $D_l$  of 40 km, reproducing the overall postseismic pattern better than a thicker lithosphere. There are a few models that produce comparable good fits to the GRACE postseismic field, and from Figure 10 it shows that these models (the model with the lowest RMSD and 5% higher) reproduce well the time series at the locations of maximum positive and negative postseismic change. The best fit has parameters  $\eta_k = 7.5 \cdot 10^{18}$  Pa s,  $\eta_m = 5 \cdot 10^{19}$  Pa s,  $D_l = 40$  km, and  $\gamma = 0.75$ , and its spatial pattern is shown in Figure 7. Compared to the sensitivity to the transient viscosity  $\eta_k$ , we see that the time series are still too short to constrain the steady state viscosity  $\eta_m$  with the same precision. The best results, however, are obtained with steady state viscosities  $\eta_m = 5 \cdot 10^{19}$  to  $7.5 \cdot 10^{19}$  Pa s. Higher viscosities have not been tested.

## 7. Localized Deformation: Afterslip

Next to distributed relaxation we test whether the observed postseismic trends can be explained using localized afterslip. We design a simple forward afterslip model by placing a few seismic point sources on the slab surface, using the SLAB 1.0 slab geometry [Hayes *et al.*, 2012]. In this way we obtain a first-order estimate of the amount and location of the slip needed to explain the far-field GPS and GRACE gravity changes within the first year after the main event. We use six scenarios where we place six dip-slip point sources along strike with a 250 km interval (Figure C1 shows the focal mechanisms for these sources), while taking constant source depths, between 15 and 65 km depth. Based on a trial and error approach, we assign the three northern sources twice the seismic moment as the three southern point sources and scale the total amount of seismic moment by maximizing the fit with 1 year of postseismic displacement at GPS site PHUK. Especially since GRACE has very little sensitivity to along-strike variations (due to the resolution of about 500 km at maximum spherical harmonic degree and order  $l_{\max} = 40$ ), there is little benefit in further optimizing the

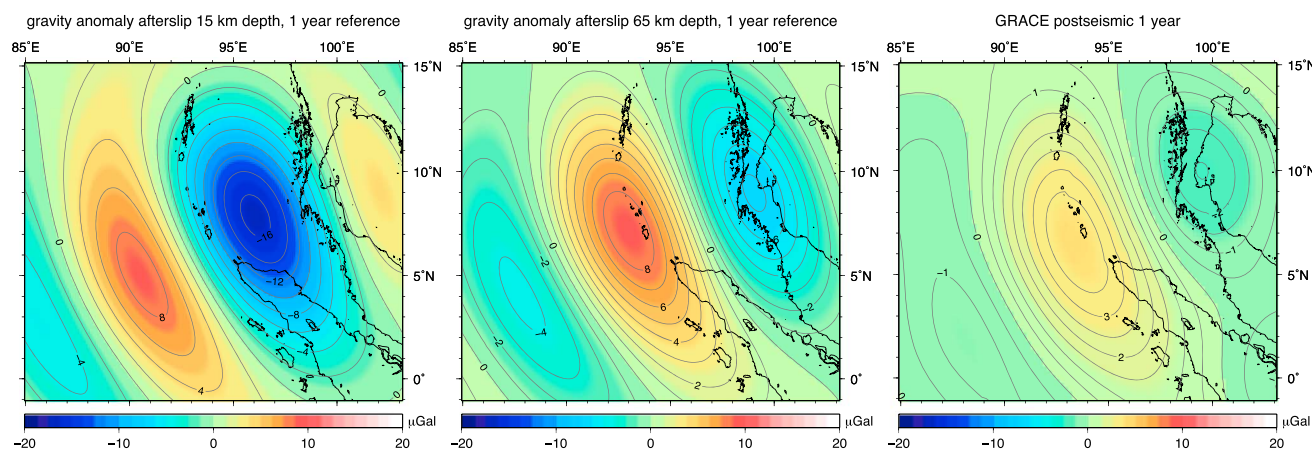


**Figure 11.** Comparison between GRACE postseismic gravity changes and forward models of afterslip that fit the postseismic GPS displacements in 2005. (left) Gravity change due to slip at 15 km depth, total aseismic moment needed for GPS fit:  $M_0 = 8.5 \cdot 10^{22}$  Nm. (middle) Gravity change due to slip at 65 km depth, total aseismic moment needed for GPS fit:  $M_0 = 2.43 \cdot 10^{22}$  Nm. (right) GRACE postseismic after 1 year (using equation (4)). All gravity anomalies are truncated at spherical harmonic degree and order  $l_{\max} = 40$ .

afterslip distribution along strike direction. We find little sensitivity to source depth as all source depths fit the horizontal 1 year GPS for all sites equally well (see Figure C1 in Appendix C), which justifies the forward model approach instead of a full inversion for slip. None of the afterslip models explains the observed subsidence (Figure 5), as all models (including those not shown with intermediate source depths) predict uplift in a broad area around sites PHUK and RYNG. Figure 11 shows a clear misfit between the modeled gravity changes of two end-member afterslip models, at 15 and 65 km depth (where intermediate depths show a gradual transition between those two) and the GRACE postseismic gravity change after 1 year. Namely, the shallow depth (15 km) afterslip model predicts a negative peak that is 6.6 times higher than what is found from GRACE and has an oceanward offset in peak location. On the other hand, the downdip afterslip model (65 km depth) agrees with GRACE with respect to the location of peak postseismic gravity changes, but this model too predicts 2.8 times too large negative gravity changes.

## 8. Discussion

Even when considering the large uncertainties in the GRACE relaxation times, GRACE observes a much slower relaxation time of the gravity field ( $\tau_{\text{in}} = 2.9$  years, at the location of largest signal) than the relaxation time in the back arc horizontal displacements as obtained with GPS ( $\tau_{\text{in}} = 0.4 - 1$  years, Figure 4). Previous studies based on maximum 4.5 years of GRACE data show estimated (exponentially decaying) trends that are almost relaxed after  $\sim 4$  years [Han et al., 2008; Hoechner et al., 2011; Tanaka and Heki, 2014]. In the same vein, de Linage et al. [2009] concluded that 26 months of postseismic gravity changes are close to the total postseismic gravity change. Based on longer time series we show that the postseismic trend in gravity due to the 2004 event is far from completed as it is still continuing in 2012, more than 7 years after the event (Figure 8).

We show that even within the first year after the 2004 earthquake, afterslip alone cannot explain the far-field GPS displacements, as afterslip models overestimate postseismic gravity changes (Figure 11). With respect to spatial patterns, shallow afterslip performs worse than slip downdip of the coseismic rupture. Our models of both shallow as well as deep afterslip predict uplift at sites where we observe postseismic subsidence. We thus conclude that the majority of gravity changes and GPS displacements should be due to volume relaxation of the viscoelastic asthenosphere [cf. Hoechner et al., 2011]. Recently, similar predominance of viscoelastic relaxation over afterslip after the 2011 Tohoku earthquake has been reported based on ocean floor displacements [Han et al., 2014; Sun et al., 2014]. Still, based on the observations from this study we cannot rule out that shallow afterslip is needed to explain displacements close to the trench. However, the difference in GPS/GRACE relaxation time is not reproduced using models that are limited to laterally uniform viscosities for the mantle, as these predict similar relaxation times for surface displacements and gravity field changes. GPS observations are best fit using asthenosphere Kelvin viscosities of around  $1 \cdot 10^{18}$  Pa s [cf. Hoechner et al., 2011], while we find that a frequently reported Kelvin viscosity of around  $\eta_k = 5 \cdot 10^{17}$  Pa s [Pollitz et al., 2006; Han et al., 2008; Panet et al., 2010; Hu and Wang, 2012] leads to too fast transients ( $\tau_{\text{in}} < 0.2$  years). Additionally, transient Kelvin viscosities are found to be below  $2.5 \cdot 10^{18}$  Pa s. Maxwell viscosities in the asthenosphere of about  $\eta_m = 7.5 \cdot 10^{18}$  Pa s lead to a rate of deformation after 7 years that coincides with that found with

GPS, in agreement with previously reported values (Table 1). On the other hand, we find a good fit for the GRACE-derived gravity changes using transient viscosities of around  $\eta_k = 7.5 \cdot 10^{18} - 1 \cdot 10^{19}$  Pa s, almost 1 order of magnitude higher than those needed to fit GPS. Similarly, we find an order of magnitude higher steady state viscosity from fitting GRACE trends:  $\eta_m = 5 \cdot 10^{19}$  to  $7.5 \cdot 10^{19}$  Pa s.

GRACE senses the largest gravity changes over the trench (where the oceanic lithosphere dips eastward), while the GPS data that we use stems from the continental Sunda plate. Therefore, we argue that GRACE and GPS actually observe relaxation in two different domains: below oceanic lithosphere (GRACE) and in the mantle wedge above the subducting oceanic slab (far-field GPS). Differences in viscosity at both sides of the subducting oceanic slab may then explain the different rates of relaxation. There are strong indications that the subducting oceanic crust transports water into the above mantle [e.g., *Billen and Gurnis*, 2001], which may lower the mantle wedge viscosity up to an order of magnitude compared to oceanic asthenosphere [*Hirth and Kohlstedt*, 2003; *Dixon et al.*, 2004; *Muto et al.*, 2013]. Additional support for low viscosities in the mantle wedge of several subduction zones are the findings of high mantle wedge temperatures [*Currie and Hyndman*, 2006], despite the fact that the underthrusting slab is cool. For the 2004 event a few studies considered an order of magnitude drop in Kelvin and Maxwell viscosities [*Pollitz et al.*, 2008] or Maxwell viscosity only [*Hu and Wang*, 2012], going from oceanic asthenosphere to the mantle wedge at opposing sides of the subducting slab. As these studies consider GPS data only, they are mostly sensitive to relaxation of the mantle wedge. Previously, *Hu et al.* [2004] reported that tide gauge observations after the great 1960 Chile earthquake could be explained when assuming an oceanic mantle Maxwell viscosity of an order of magnitude higher than that of the mantle wedge, while surface velocities at the continent are almost unaffected.

*Rousset et al.* [2012] found spatial varying characteristic relaxation times (exponential) based on more than 10 years of postseismic displacements after the 1999 Chi-Chi earthquake, Taiwan, with increasing relaxation times for far-field sites. They show a coupled afterslip and viscoelastic model, implementing a Maxwell rheology and including a local low-viscosity zone, that can reproduce faster transients near the fault. In contrast to *Rousset et al.* [2012], we find fast transients in the far-field displacements and slow transients in the long-wavelength part of the gravity changes. In our study, the combination of both afterslip and viscoelastic relaxation is an unlikely cause for the spatially changing relaxation times since the gravity data rule out the scenario that afterslip explains the early far-field GPS displacements. In case a minor part of the postseismic signal is due to afterslip, a likely result is that afterslip contributes mainly to the early stages of postseismic relaxation. Even though we did not model the combination of afterslip and mantle relaxation, it is unlikely that our hypothesis of lateral viscosity contrasts is affected by the presence of afterslip, since far-field surface displacements and gravity changes due to localized deformation will show the same temporal behavior. However, only distributed deformation such as mantle relaxation allows for different rates of relaxation in distinct areas.

The next step will be the confrontation of models that include slab geometry and lateral variations in viscosity and density to both land displacements and gravity field changes, preferably including a direct coupling of afterslip and viscoelastic creep [e.g., *Hu and Wang*, 2012; *Rollins et al.*, 2015]. This combination can lead to better understanding of the viscosity contrast at both sides of the subducting slab. Furthermore, the presence of a cool subducting slab may also affect the relaxation times. Such a model will also affect the displacements at our GPS locations [*Pollitz et al.*, 2008] and may potentially improve the fit at those locations where our radially symmetric models perform less well (such as at sites PHUK and SRIS). Interpretation of postseismic relaxation with power law rheologies still remains an open issue for subduction zone earthquakes. Power law rheology applied to megathrust earthquakes deserves a more rigorous examination in order to integrate phenomenological deductions of upper mantle viscosity with knowledge of rock deformation from the lab. However, this results in adding a large number of degrees of freedom, and as extrapolations from rock mechanical experiments are required, power law empirical relations come with major uncertainties. In our perspective, geophysical observations can be used to test these extrapolations. On the other hand, it opens a possibility to study to what extent the inferred low viscosities are a result of changes in stress and how these may differ from long-term (higher) viscosities [*Freed et al.*, 2010], as the (effective) viscosities that we find may depend on the size of the earthquake and resolution of the observations [*Riva and Govers*, 2009]. Power law dependence on stress can lead to temporal and spatial localization of low effective viscosities, which may have an effect on characteristic relaxation times in the observations. We expect that the spatial asymmetry



in observed relaxation times cannot be explained by stress dependence alone, since the largest region with high stress changes are to be expected in the oceanic asthenosphere [see, e.g., Pollitz *et al.*, 2008, Figures 13 and 14]. Yet while linear viscoelastic rheologies are very simple, if we can fully explain the available observations with these, there may be no need for further rheological complexity from the perspective of these data. Transient (recoverable) creep is likely an essential feature in interpreting postseismic relaxation as most Sumatra-Andaman studies require transient viscosities to explain the data, and also (unrecoverable) steady state creep derived from power law rheology fails to explain postseismic deformation in a continental setting [Freed *et al.*, 2012]. Furthermore, since the 2004 earthquake is relatively recent, there is a possibility that what we interpret as steady state deformation is yet another transient, and thus recoverable, phase, for which an extended Burgers rheology could be adopted. As the postseismic deformation and gravity field changes since the Sumatra-Andaman earthquake are still ongoing processes, longer time spans of observations will increase the sensitivity to transient and steady state low-viscosity zones. The remaining years of the GRACE mission and its follow-up mission can further constrain the rate of relaxation after the huge 2004 Sumatra-Andaman earthquake and may also shed light on relaxation following other very large ( $M_w > 9$ ) earthquakes such as the 2011 Tohoku earthquake.

## 9. Conclusions

We use both GPS-observed surface displacements and GRACE gravity changes to investigate postseismic relaxation after the 2004 Sumatra-Andaman earthquake, both in continental and oceanic areas.

1. We show that localized deformation in the form of afterslip cannot be the dominant factor in the first year of postseismic relaxation, as the amount of afterslip needed to explain the far-field GPS observations overestimates the low-degree gravity changes by at least a factor 2.8 and the uplift predicted by afterslip models does not match the observed subsidence. However, we show that viscoelastic mantle relaxation (modeled with a biviscous Burgers rheology) can explain the observed postseismic relaxation. Nevertheless, we cannot explain the far-field GPS displacements and GRACE gravity changes with a single set of rheological parameters.
2. Thanks to the extended amount of postseismic GRACE gravity data (>7 years), the relaxation rate of the postseismic gravity field can be constrained better than in previous studies. A new observation is that the relaxation of the gravity field at GRACE resolution is much slower than what GPS observes over land in the back arc. In other words, in the GPS displacements we see a larger contrast between early and later displacement rates than we see in the GRACE postseismic time series. We suggest that relaxation in the oceanic asthenosphere (over which GRACE measures the largest changes) and continental asthenosphere (sampled by GPS) happens at different rates. Since localized deformation will lead to the same temporal behavior in the affected area, we argue that distributed deformation should be responsible for contrasts in the rate of relaxation. In that case we need an order of magnitude higher viscosity in the oceanic asthenosphere compared to the mantle wedge. Knowing that subducting sediments and oceanic crust transport water deep into the overlying mantle by dehydration, makes it likely that the mantle wedge is significantly weaker than oceanic asthenosphere as water lowers the viscosity of mantle rocks [Hirth and Kohlstedt, 2003]. We show that satellite gravimetry is currently the only geodetic technique that has shown to be quantitatively sensitive to this viscosity contrast. Moreover, this observation has implications for modeling postseismic relaxation as well, as it suggests that the observed relaxation cannot be captured by the commonly used 1-D viscosity profiles.

## Appendix A: Transient Normal Modes

The normal modes model as used in this study analytically computes the Earth's responses due to loading [e.g., Sabadini and Vermeersen, 2004], such as due to earthquakes [Piersanti *et al.*, 1995]. Normal modes represent standing waves (or free oscillations) in terms of Earth deformation that arise due to instantaneous loading and are dependent on the internal structure of the Earth. The concept of free oscillations of a sphere is an important concept in both seismology (as the Earth's normal modes can be observed after large earthquakes) and the quasi-static deformation of a spherical Earth. Here quasi-static deformation can be modeled as an oscillation with an infinite period [Ben-Menahem and Singh, 1981]. Here we briefly describe the Burgers rheology and its implementation in the normal mode approach.



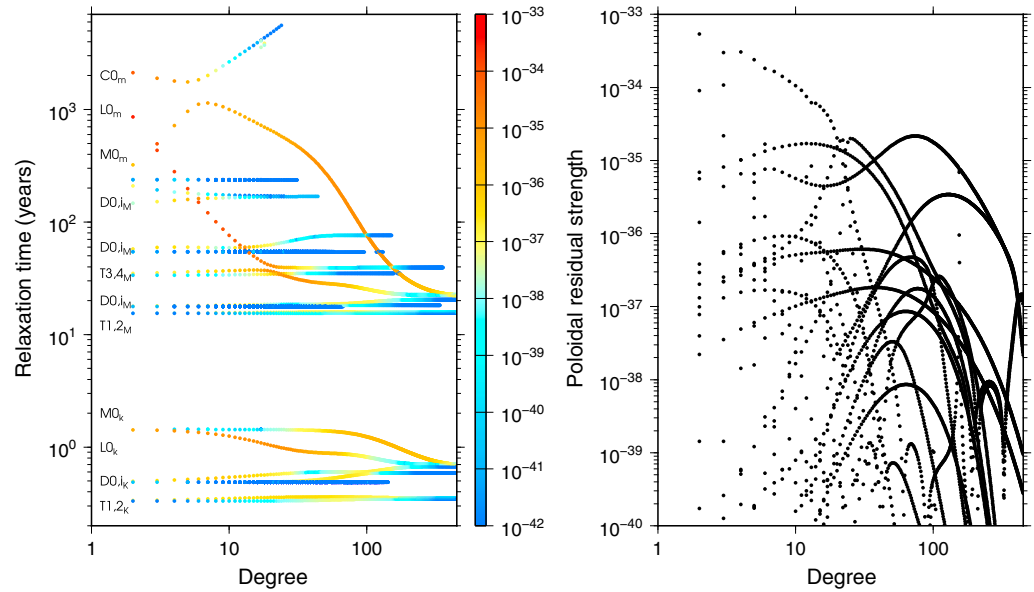


**Figure A1.** Modes associated with the best fit GPS model with parameters: asthenosphere viscosities  $\eta_k = 1 \cdot 10^{18} / \eta_m = 7.5 \cdot 10^{18}$  Pa s, shear modulus ratio  $\gamma = 0.33$ , and lithospheric thickness  $D_l = 60$  km, for the remainder of the parameters, see Table 2. (left) Modes and poloidal residuals for a seismic point source with an  $M_0$  of 1 Nm at 30 km depth and a dip of  $12^\circ$ . On the x axis degree and on y axis the relaxation time, colors denote the absolute residual strength. (right) Same as Figure A1 (left) but with absolute residual strength on the y axis. Modes found include C0 core mode, M0 free surface modes, L0 lithosphere modes, Ti coupled transient modes, and bands of dilation modes  $DO_{...}$ . Subscripts denote m Maxwell or k Kelvin modes. Note that buoyancy modes are not searched for since these have very long relaxation times. Lithosphere L0 modes are strongest for the very low degrees, whereas free surface modes M0 dominate in the higher degrees. Maximum degree computed  $l_{\max} = 450$ .

The simplest rheological model that incorporates both elastic, transient creep, and steady state creep is the biviscous Burgers rheology [Peltier *et al.*, 1981]. The Burgers model essentially extends the common Maxwell model (that models elastic deformation and steady state creep) by taking a Maxwell element and coupling this in series with a Kelvin element (that models transient creep) [Burgers, 1939]. The Maxwell element is schematically represented by a spring with rigidity  $\mu_m$  in series with a dashpot with viscosity  $\eta_m$ ; the Kelvin element consists of a spring with rigidity  $\mu_k$  coupled in parallel with a dashpot with viscosity  $\eta_k$  (see Figure 1). As the newly introduced spring is coupled in parallel by a dashpot, it does not introduce any elastic deformation, but it allows for an anelastic transient viscoelastic deformation that causes a fast relaxation quickly after the application of a load (such as the occurrence of an earthquake). The influence of the transient deformation then diminishes, since it allows for only limited strain as effective viscosity increases with time [Rümpker and Wolf, 1996]. Subsequently, the Maxwell relaxation becomes dominant at longer timescales. In normal modes models the stress-strain relations are written in the Laplace domain, which in the case of a linear rheology (e.g., Maxwell, Burgers) can be written as follows [Yuen and Peltier, 1982]

$$\tilde{\sigma}_{ij}(s) = 2\tilde{\mu}(s)\tilde{\epsilon}_{ij}(s) + \tilde{\lambda}(s) \sum_{k=1}^3 \tilde{\epsilon}_{kk}(s)\delta_{ij} \quad (A1)$$

where  $\sigma_{ij}$  is deviatoric stress,  $\epsilon_{ij}$  is deviatoric strain,  $\delta$  denotes the Kronecker delta tensor,  $s$  is the inverse relaxation time, and the tilde denotes the Laplace transform of the original variables. The rheological properties are now condensed in the so-called compliances  $\tilde{\mu}(s)$  and  $\tilde{\lambda}(s)$ . For a Burgers model the expressions in the Laplace domain are given by Peltier *et al.* [1986]

$$\tilde{\mu}(s) = \frac{s \left( s + \frac{\mu_k}{\eta_k} \right) \mu_m}{s^2 + s \left( \frac{\mu_m + \mu_k}{\eta_k} + \frac{\mu_m}{\eta_m} \right) + \frac{\mu_m \mu_k}{\eta_m \eta_k}} \quad (A2)$$

$$\tilde{\lambda}(s) = \frac{\lambda s^2 + s \left( \left( \frac{\mu_m + \mu_k}{\eta_k} + \frac{\mu_m}{\eta_m} \right) \left( \lambda + 2/3 \mu_m \right) - 2/3 \frac{\mu_k \mu_m}{\eta_k} \right) + \frac{\mu_k \mu_m (\lambda + 2/3 \mu_m)}{\eta_m \eta_k}}{s^2 + s \left( \frac{\mu_m + \mu_k}{\eta_k} + \frac{\mu_m}{\eta_m} \right) + \frac{\mu_m \mu_k}{\eta_m \eta_k}} \quad (A3)$$

In the normal mode approach, the viscoelastic response of an Earth model due to a load comprises several modes that represent the interaction between adjacent layers. Depending on the chosen rheology and the number of layers in the model a specific number of modes can be expected (see, e.g., *Sabadini and Vermeersen* [2004], for a detailed discussion). For models including compressibility of the solid Earth a denumerably infinite amount of dilatation modes is present as well [*Han and Wahr*, 1995; *Vermeersen et al.*, 1996]. Since the Burgers model is an extension of the Maxwell model (with addition of a Kelvin element), the modes that are applicable to Maxwell models are present as well, next to a number of new modes. Figure A1 displays the modes resulting for the best GPS fit model, together with the strength of these modes for poloidal deformation of a source with an  $M_0$  of 1 Nm at 30 km depth and a dip of  $12^\circ$ . We search for modes per spherical harmonic degree, but do not track all modes continuously for increasing degrees when the residuals drop below a small value. An additional check consists in verifying the absence of oscillations in the far-field deformation field (normally caused by gaps in modes or anomalies in residual values).

### Appendix B: Sensitivity to Changes in Rheological Parameters

We test the sensitivity of horizontal displacement due to variation in rheological parameters at the locations of GPS sites CPNT and OTRI. Figure B1 shows that variation in transient asthenosphere viscosity  $\eta_k$  mainly affects the initial deformation rate: the lower is  $\eta_k$ , the faster the initial postseismic deformation. On the other hand, variation in steady state asthenosphere viscosity  $\eta_m$  has little influence on the initial deformation as

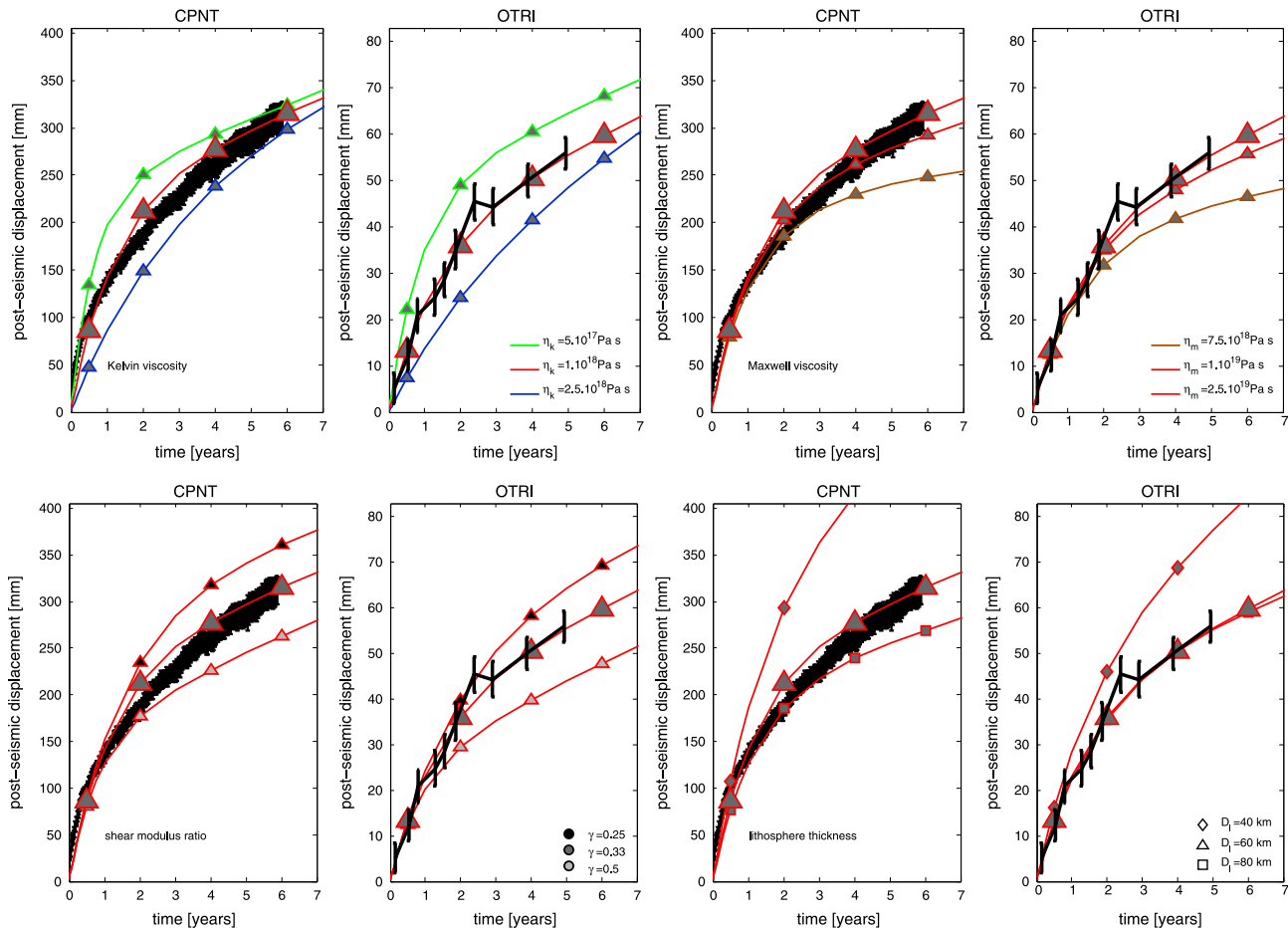


**Figure B1.** Sensitivity of horizontal displacements due to variations in rheological parameters at the locations of GPS sites CPNT and OTRI. All variations are shown with respect to the best fit model with parameters: asthenosphere viscosities  $\eta_k = 1 \cdot 10^{18} / \eta_m = 7.5 \cdot 10^{18}$  Pa s, shear modulus ratio  $\gamma = 0.33$  and lithospheric thickness  $D_l = 60$  km. (top left) Variation in transient asthenosphere viscosity  $\eta_k$ . (top right) Variation in steady state asthenosphere viscosity  $\eta_m$ . (bottom left) Variation of shear modulus ratio  $\gamma (= \frac{\mu_k}{\mu_m})$ . (bottom right) Variation in the elastic thickness  $D_l$ . GPS time series are shown with  $1\sigma$  error bars.

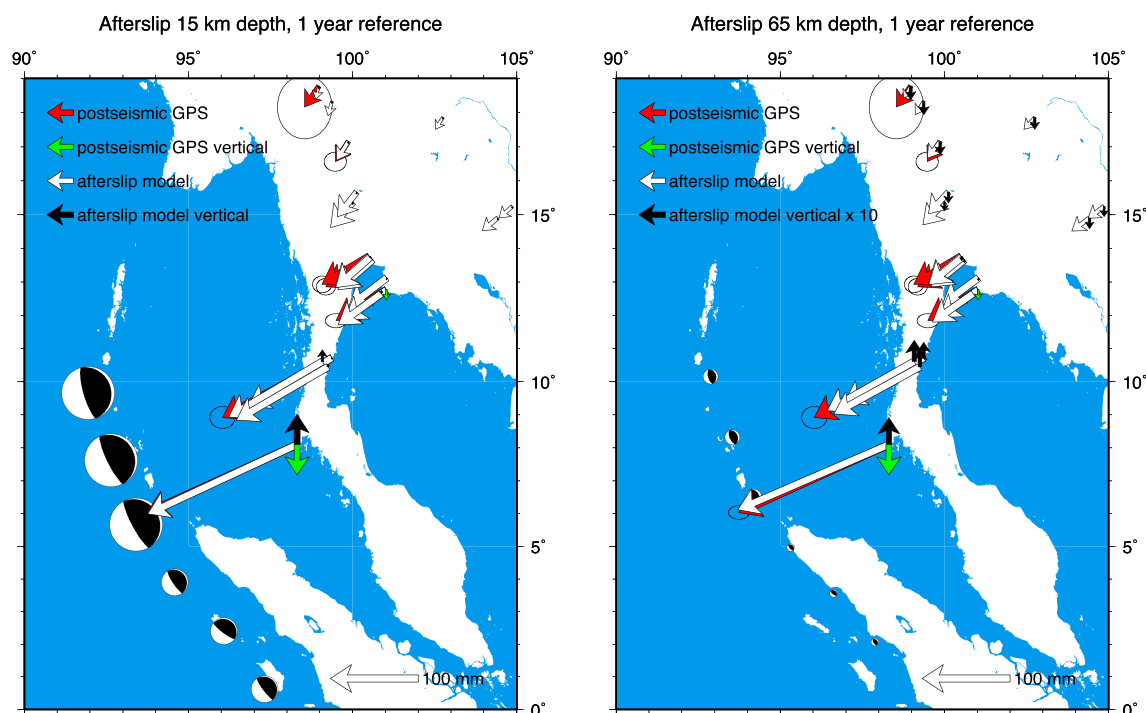


**Figure C1.** Comparison between 1 year of GPS postseismic displacements and forward models of afterslip. Horizontal GPS vectors are identical to the 1 year postseismic displacements, vertical GPS vectors are based on the logarithmic fit to the vertical GPS displacements. (left) Displacements due to dip slip at 15 km depth. (right) Displacements due to dip slip at 65 km depth. Note that for the afterslip model with slip at 65 km depth, the modeled vertical displacements are scaled by a factor of 10. Point sources as used in the modeling are shown as focal mechanisms, where the symbol size is scaled by seismic moment, not by magnitude.

#### Acknowledgments

We thank the reviewers Sylvain Barbot, Eric Hetland, and the Associate Editor Laura Wallace for their comments and suggestions which have resulted in a substantially improved manuscript. This paper benefited from discussions with Auke Barnhoorn. Taco Broerse acknowledges financial support from the SRON/NWO grant GO-AO/20 and ISES. The GPS data used in this paper were collected as part of our cooperation in the EU-ASEAN SEAMERGES (2004–2006) and GEO2TECDI-1/2 projects (2009–2013). We like to extend our special thanks to the Royal Thai Survey Department (RTSD) and Chulalongkorn University (CHULA) from Thailand and the National Institute of Information and Communications Technology (NICT) from Japan for their valuable data contributions. The GPS data acquisition and research were also funded by grants from the NWO User Support Programme Space Research (2007–2014). The authors contributed in the following proportions to the (1) conception and funding of the project, (2) project design, (3) data acquisition and processing, (4) modeling, and (5) manuscript preparation (%): T.B. (0;60;30;100;55), R.R. (50;20;0;0;20), W.S. (0;0;70;0;5), R.G. (30;10;0;0;10), and B.V. (20;10;0;0;10).

can be seen in Figure B1 (top right). The influence of the steady state asthenosphere viscosity can be seen in the slope of the deformation at later stages: a lower  $\eta_m$  results in higher deformation rates a few years after the seismic event. As Figure B1 (bottom left) shows, variation of shear modulus ratio  $\gamma (= \frac{\mu_k}{\mu_m})$  changes the amount of transient deformation: a weaker Kelvin element (lower  $\gamma$ ) results in a more transient deformation. Note that the deformation rate after 7 years is hardly affected. Variation in the elastic thickness  $D_l$  affects the amount of deformation, the thinner the lithosphere, the more deformation is predicted, Figure B1 (bottom right). However, the relative effect is not the same for all distances to the rupture: for nearby sites (CPNT) the effect is stronger than for very far-field sites (OTRI).

#### Appendix C: Afterslip Fit With GPS Displacements

Figure C1 compares the 1 year GPS postseismic displacements (only available at permanent sites) with the forward models of afterslip. Here we show the two end-member models; in the left panel the fit for the model with dip slip at 15 km depth, with a total aseismic moment:  $M_0 = 8.5 \cdot 10^{22}$  Nm; in the right panel the fit for dip slip at 65 km depth, with a total aseismic moment:  $M_0 = 2.43 \cdot 10^{22}$  Nm. None of the forward afterslip models provides the observed subsidence.

#### References

- Altamimi, Z., X. Collilieux, J. Legrand, B. Garayt, and C. Boucher (2007), ITRF2005: A new release of the international terrestrial reference frame based on time series of station positions and Earth orientation parameters, *J. Geophys. Res.*, *112*, B09401, doi:10.1029/2007JB004949.
- Barbot, S., Y. Fialko, and Y. Bock (2009), Postseismic deformation due to the  $M_w$  6.0 2004 Parkfield earthquake: Stress-driven creep on a fault with spatially variable rate-and-state friction parameters, *J. Geophys. Res.*, *114*, B07405, doi:10.1029/2008JB005748.
- Ben-Menahem, A., and S. Singh (1981), *Seismic Waves and Sources*, Springer, New York.
- Bettadpur, S. (2012), Insights into the Earth system mass variability from CSR-RL05 GRACE gravity fields. Geophysical Research Abstracts, Vol. 14, EGU2012-6409 presented at EGU General Assembly 2012, held 22–27 April, 2012 in Vienna, Austria.
- Billham, R., R. Engdahl, N. Feldl, and S. Satyabala (2005), Partial and complete rupture of the Indo-Andaman plate boundary 1847–2004, *Seismol. Res. Lett.*, *76*(3), 299–311.
- Billen, M. I., and M. Gurnis (2001), A low viscosity wedge in subduction zones, *Earth Planet. Sci. Lett.*, *193*(1), 227–236.

- Broerse, D., L. Vermeersen, R. Riva, and W. van der Wal (2011), Ocean contribution to co-seismic crustal deformation and geoid anomalies: Application to the 2004 December 26 Sumatra-Andaman earthquake, *Earth Planet. Sci. Lett.*, *305*(3–4), 341–349, doi:10.1016/j.epsl.2011.03.011.
- Broerse, T., R. Riva, and B. Vermeersen (2014), Ocean contribution to seismic gravity changes: The sea level equation for seismic perturbations revisited, *Geophys. J. Int.*, *199*(2), 1094–1109.
- Burgers, J. (1939), *Mechanical Considerations-Model Systems-Phenomenological Theories of Relaxation and Viscosity, First Report on Viscosity and Plasticity*, Nordemann Publ. Comp., New York.
- Bürgmann, R., and G. Dresen (2008), Rheology of the lower crust and upper mantle: Evidence from rock mechanics, geodesy, and field observations, *Annu. Rev. Earth Planet. Sci.*, *36*, 531–567.
- Cambiotti, G., A. Bordon, R. Sabadini, and L. Colli (2011), GRACE gravity data help constraining seismic models of the 2004 Sumatran earthquake, *J. Geophys. Res.*, *116*, B10403, doi:10.1029/2010JB007848.
- Chen, J., C. Wilson, B. Tapley, and S. Grand (2007), GRACE detects coseismic and postseismic deformation from the Sumatra-Andaman earthquake, *Geophys. Res. Lett.*, *34*, L13302, doi:10.1029/2007GL030356.
- Chlieh, M., et al. (2007), Coseismic slip and afterslip of the great  $M_w$  9.15 Sumatra-Andaman earthquake of 2004, *Bull. Seismol. Soc. Am.*, *97*(1A), S152–S173.
- Chopra, P. N. (1997), High-temperature transient creep in olivine rocks, *Tectonophysics*, *279*(1), 93–111.
- Currie, C. A., and R. D. Hyndman (2006), The thermal structure of subduction zone back arcs, *J. Geophys. Res.*, *111*, B08404, doi:10.1029/2005JB004024.
- de Linage, C., L. Rivera, J. Hinderer, J. Boy, Y. Rogister, S. Lambotte, and R. Biancale (2009), Separation of coseismic and postseismic gravity changes for the 2004 Sumatra-Andaman earthquake from 4.6 yr of GRACE observations and modelling of the coseismic change by normal-modes summation, *Geophys. J. Int.*, *176*(3), 695–714.
- Dixon, J. E., T. H. Dixon, D. Bell, and R. Malservici (2004), Lateral variation in upper mantle viscosity: Role of water, *Earth Planet. Sci. Lett.*, *222*(2), 451–467.
- Dziewonski, A., and D. Anderson (1981), Preliminary reference Earth model, *Phys. Earth Planet. Inter.*, *25*(4), 297–356.
- Faul, U., and I. Jackson (2005), The seismological signature of temperature and grain size variations in the upper mantle, *Earth Planet. Sci. Lett.*, *234*(1), 119–134.
- Freed, A., T. Herring, and R. Bürgmann (2010), Steady-state laboratory flow laws alone fail to explain postseismic observations, *Earth Planet. Sci. Lett.*, *300*(1), 1–10.
- Freed, A., G. Hirth, and M. Behn (2012), Using short-term postseismic displacements to infer the ambient deformation conditions of the upper mantle, *J. Geophys. Res.*, *117*, B01409, doi:10.1029/2011JB008562.
- Gahalaut, V., B. Nagarajan, J. Catherine, and S. Kumar (2006), Constraints on 2004 Sumatra-Andaman earthquake rupture from GPS measurements in Andaman-Nicobar Islands, *Earth Planet. Sci. Lett.*, *242*(3), 365–374.
- Gribb, T. T., and R. F. Cooper (1998), Low-frequency shear attenuation in polycrystalline olivine: Grain boundary diffusion and the physical significance of the Andrade model for viscoelastic rheology, *J. Geophys. Res.*, *103*(B11), 27,267–27,279.
- Han, D., and J. Wahr (1995), The viscoelastic relaxation of a realistically stratified Earth, and a further analysis of postglacial rebound, *Geophys. J. Int.*, *120*(2), 287–311.
- Han, S., J. Sauber, S. Luthcke, C. Ji, and F. Pollitz (2008), Implications of postseismic gravity change following the great 2004 Sumatra-Andaman earthquake from the regional harmonic analysis of GRACE intersatellite tracking data, *J. Geophys. Res.*, *113*, B11413, doi:10.1029/2008JB005705.
- Han, S.-C., R. Riva, J. Sauber, and E. Okal (2013), Source parameter inversion for recent great earthquakes from a decade-long observation of global gravity fields, *J. Geophys. Res. Solid Earth*, *41*, L060905, doi:10.1002/jgrb.50116.
- Han, S.-C., J. Sauber, and F. Pollitz (2014), Broad-scale postseismic gravity change following the 2011 Tohoku-Oki earthquake and implication for deformation by viscoelastic relaxation and afterslip, *Geophys. Res. Lett.*, *41*, 5797–5805, doi:10.1002/2014GL060905.
- Hayes, G. P., D. J. Wald, and R. L. Johnson (2012), Slab1.0: A three-dimensional model of global subduction zone geometries, *J. Geophys. Res.*, *117*, B01302, doi:10.1029/2011JB008524.
- Helmstetter, A., and B. E. Shaw (2009), Afterslip and aftershocks in the rate-and-state friction law, *J. Geophys. Res.*, *114*, B01308, doi:10.1029/2007JB005077.
- Hetland, E., and B. Hager (2006), The effects of rheological layering on post-seismic deformation, *Geophys. J. Int.*, *166*(1), 277–292.
- Hirth, G., and D. Kohlstedt (2003), Rheology of the upper mantle and the mantle wedge: A view from the experimentalists, in *Inside the Subduction Factory*, edited by J. Eiler, pp. 83–105, AGU, Washington, D. C.
- Hoechner, A., S. Sobolev, I. Einarsson, and R. Wang (2011), Investigation on afterslip and steady state and transient rheology based on postseismic deformation and geoid change caused by the Sumatra 2004 earthquake, *Geochim. Geophys. Geosyst.*, *12*, Q07010, doi:10.1029/2010GC003450.
- Hsu, Y., M. Simons, J. Avouac, J. Galetzka, K. Sieh, M. Chlieh, D. Natawidjaja, L. Prawirodirdjo, and Y. Bock (2006), Frictional afterslip following the 2005 Nias-Simeulue earthquake, Sumatra, *Science*, *312*(5782), 1921–1926.
- Hu, Y., and K. Wang (2012), Spherical-Earth finite element model of short-term postseismic deformation following the 2004 Sumatra earthquake, *J. Geophys. Res.*, *117*, B05404, doi:10.1029/2012JB009153.
- Hu, Y., K. Wang, J. He, J. Klotz, and G. Khazaradze (2004), Three-dimensional viscoelastic finite element model for postseismic deformation of the great 1960 Chile earthquake, *J. Geophys. Res.*, *109*, B12403, doi:10.1029/2004JB003163.
- Hughes, K., T. Masterlark, and W. Mooney (2010), Poroelastic stress-triggering of the 2005 M8.7 Nias earthquake by the 2004 M9.2 Sumatra-Andaman earthquake, *Earth Planet. Sci. Lett.*, *293*(3), 289–299.
- Karato, S. (2011), Water distribution across the mantle transition zone and its implications for global material circulation, *Earth Planet. Sci. Lett.*, *301*(3), 413–423.
- Lakki, A., R. Schaller, C. Carry, and W. Benoit (1998), High temperature anelastic and viscoplastic deformation of fine-grained MgO-doped  $\text{Al}_2\text{O}_3$ , *Acta Mater.*, *46*(2), 689–700.
- Melini, D., G. Spada, and A. Piersanti (2010), A sea level equation for seismic perturbations, *Geophys. J. Int.*, *180*(1), 88–100.
- Muto, J., B. Shibazaki, Y. Ito, T. Iinuma, M. Ohzono, T. Matsumoto, and T. Okada (2013), Two-dimensional viscosity structure of the northeastern Japan islands arc-trench system, *Geophys. Res. Lett.*, *40*, 4604–4608, doi:10.1002/grl.50906.
- Ogawa, R., and K. Heki (2007), Slow postseismic recovery of geoid depression formed by the 2004 Sumatra-Andaman Earthquake by mantle water diffusion, *Geophys. Res. Lett.*, *34*, L06313, doi:10.1029/2007GL029340.
- Ozawa, S., T. Nishimura, H. Munekane, H. Suito, T. Kobayashi, M. Tobita, and T. Imakiire (2012), Preceding, coseismic, and postseismic slips of the 2011 Tohoku earthquake, Japan, *J. Geophys. Res.*, *117*, B07404, doi:10.1029/2011JB009120.

- Panet, I., F. Pollitz, V. Mikhailov, M. Diament, P. Banerjee, and K. Grijalva (2010), Upper mantle rheology from GRACE and GPS postseismic deformation after the 2004 Sumatra-Andaman earthquake, *Geochim. Geophys. Geosyst.*, *11*, Q06008, doi:10.1029/2009GC002905.
- Paul, J., A. Lowry, R. Bilham, S. Sen, and R. Smalley Jr. (2007), Postseismic deformation of the Andaman Islands following the 26 December, 2004 Great Sumatra-Andaman earthquake, *Geophys. Res. Lett.*, *34*, L19309, doi:10.1029/2007GL031024.
- Paul, J., C. Rajendran, A. Lowry, V. Andrade, and K. Rajendran (2012), Andaman postseismic deformation observations: Still slipping after all these years?, *Bull. Seismol. Soc. Am.*, *102*(1), 343–351.
- Peltier, W., P. Wu, and D. Yuen (1981), The viscosities of the Earth's mantle, *Anelastic. Earth Geodyn. Ser.*, *4*, 59–77.
- Peltier, W., R. Drummond, and A. Tushingham (1986), Post-glacial rebound and transient lower mantle rheology, *Geophys. J. R. Astron. Soc.*, *87*(1), 79–116.
- Perfettini, H., and J. Avouac (2004), Postseismic relaxation driven by brittle creep: A possible mechanism to reconcile geodetic measurements and the decay rate of aftershocks, application to the Chi-Chi earthquake, Taiwan, *J. Geophys. Res.*, *109*, B02304, doi:10.1029/2003JB002488.
- Perfettini, H., and J. Avouac (2007), Modeling afterslip and aftershocks following the 1992 Landers earthquake, *J. Geophys. Res.*, *112*, B07409, doi:10.1029/2006JB004399.
- Piersanti, A., G. Spada, R. Sabadini, and M. Bonafede (1995), Global post-seismic deformation, *Geophys. J. Int.*, *120*(3), 544–566.
- Pollitz, F., R. Bürgmann, and P. Banerjee (2006), Post-seismic relaxation following the great 2004 Sumatra-Andaman earthquake on a compressible self-gravitating Earth, *Geophys. J. Int.*, *167*(1), 397–420.
- Pollitz, F., P. Banerjee, K. Grijalva, B. Nagarajan, and R. Bürgmann (2008), Effect of 3-D viscoelastic structure on post-seismic relaxation from the 2004  $M = 9.2$  Sumatra earthquake, *Geophys. J. Int.*, *173*(1), 189–204.
- Ray, R., and S. Luthcke (2006), Tide model errors and GRACE gravimetry: Towards a more realistic assessment, *Geophys. J. Int.*, *167*(3), 1055–1059.
- Riva, R., and R. Govers (2009), Relating viscosities from postseismic relaxation to a realistic viscosity structure for the lithosphere, *Geophys. J. Int.*, *176*(2), 614–624.
- Rollins, C., S. Barbot, and J.-P. Avouac (2015), Postseismic deformation following the 2010  $M = 7.2$  El Mayor-Cucapah earthquake: Observations, kinematic inversions, and dynamic models, *Pure Appl. Geophys.*, *172*, 1305–1358.
- Rousset, B., S. Barbot, J.-P. Avouac, and Y.-J. Hsu (2012), Postseismic deformation following the 1999 Chi-Chi earthquake, Taiwan: Implication for lower-crust rheology, *J. Geophys. Res.*, *117*, B12405, doi:10.1029/2012JB009571.
- Rümpker, G., and D. Wolf (1996), Viscoelastic relaxation of a Burgers half-space: Implications for the interpretation of the Fennoscandian uplift, *Geophys. J. Int.*, *124*(2), 541–555.
- Sabadini, R., and B. Vermeersen (2004), *Global Dynamics of the Earth: Applications of Normal Mode Relaxation Theory to Solid-Earth Geophysics*, Kluwer Acad. Publ., Dordrecht, Netherlands.
- Savage, J., J. Svarc, and S.-B. Yu (2007), Postseismic relaxation and aftershocks, *J. Geophys. Res.*, *112*, B06406, doi:10.1029/2006JB004584.
- Scholz, C. (1998), Earthquakes and friction laws, *Nature*, *391*(6662), 37–42.
- Simons, W., et al. (2007), A decade of GPS in Southeast Asia: Resolving Sundaland motion and boundaries, *J. Geophys. Res.*, *112*, B06420, doi:10.1029/2005JB003868.
- Smylie, D., and L. Mansinha (1971), The elasticity theory of dislocations in real Earth models and changes in the rotation of the Earth, *Geophys. J. R. Astron. Soc.*, *23*(3), 329–354.
- Sun, T., et al. (2014), Prevalence of viscoelastic relaxation after the 2011 Tohoku-oki earthquake, *Nature*, *514*, 84–86.
- Tanaka, Y., and K. Heki (2014), Long- and short-term postseismic gravity changes of megathrust earthquakes from satellite gravimetry, *Geophys. Res. Lett.*, *41*(15), 5451–5456, doi:10.1002/2014GL060559.
- Vermeersen, L., and R. Sabadini (1997), A new class of stratified viscoelastic models by analytical techniques, *Geophys. J. Int.*, *129*(3), 531–570.
- Vermeersen, L., R. Sabadini, and G. Spada (1996), Compressible rotational deformation, *Geophys. J. Int.*, *126*(3), 735–761.
- Vigny, C., et al. (2005), Insight into the 2004 Sumatra-Andaman earthquake from GPS measurements in southeast Asia, *Nature*, *436*(7048), 201–206.
- Wang, K., Y. Hu, and J. He (2012), Deformation cycles of subduction earthquakes in a viscoelastic Earth, *Nature*, *484*, 327–332.
- Yuen, D., and W. Peltier (1982), Normal modes of the viscoelastic Earth, *Geophys. J. R. Astron. Soc.*, *69*(2), 495–526.
- Zumberge, J., M. Heflin, D. Jefferson, M. Watkins, and F. Webb (1997), Precise point positioning for the efficient and robust analysis of GPS data from large networks, *J. Geophys. Res.*, *102*(B3), 5005–5017.